Research Article

Wenrong Si, Yiru Shou, Dengfeng Ju, Hui Deng, Sen Qian, Yingjie Gu, and Jian Yang*

Computational analysis of reconstructing current and sag of three-phase overhead line based on the TMR sensor array

https://doi.org/10.1515/phys-2023-0143
received August 30, 2023; accepted October 31, 2023

Abstract: The development of overhead lines has met the electricity demand of the rapidly developing society. However, the large-scale installation of overhead lines and the natural environmental differences in different regions increase the complexity of the real-time management of the lines. To improve the efficiency of line management, this article constructs a theoretical and simplified electromagnetic field model of 500 kV three-phase overhead lines and studies the method of monitoring the current-sag state of the lines based on analyzing the distribution of magnetic field intensity under the three-phase overhead lines. Moreover, the placement of the tunneling magnetoresistance (TMR) sensor array was analyzed, and the current and sag reconstruction algorithm of the line was further proposed. The calculation results show that the simplified magnetic field model is accurate in most areas under the overhead line. The comparison of condition number and sensor position sensitivity value on sensor placement evaluation shows that the sensor position sensitivity value is more comprehensive, and it is recommended to use dual-axis TMR magnetic sensors. The relative error of the line sag calculated by the proposed TMR sensor array and algorithm is less than 3% and 4% for balanced and unbalanced three-phase line currents, respectively.

Keywords: overhead line, magnetoresistive sensor placement, current-sag monitoring, inverse calculation

*** Corresponding author: Jian Yang,** MOE Key Laboratory of Thermo-Fluid Science and Engineering, Xi'an Jiaotong University, Xi'an 710049, China, e-mail: yangjian81@mail.xjtu.edu.cn, fax: +86 (29) 82663222
Wenrong Si, Yiru Shou: State Grid Shanghai Municipal Electrical Power Company, Shanghai 200122, China
Dengfeng Ju, Hui Deng, Sen Qian: Global Energy Interconnection Research Institute Co., Ltd., Beijing 102209, China
Yingjie Gu: MOE Key Laboratory of Thermo-Fluid Science and Engineering, Xi'an Jiaotong University, Xi'an 710049, China

Nomenclature

B	magnetic field intensity
C	intermediate variable
cond	condition number
d	vertical spacing of sensors on a detection rod
e	Euclidean distance (target function)
G	position coefficient matrix
H	line suspension point height from the ground
I	conductor current
L	line span
l	the integral path of the curve where the wire is located
M	number of detection rods
N	number of sensors on a detection rod
n	number of overhead lines
P	spatial point
p	horizontal spacing of adjacent detection rods
ps	sensor position sensitivity value
Q	infinitesimal conductor location
$\vec{r}$	position vector
S	sensor
S_{set}	sag range
sag	line sag
T	detection rod
t	time

Greek letters

α	catenary coefficient
δ	relative error of magnetic field intensity
ε	tolerance condition
μ_0	vacuum permeability
ξ	coordinate direction
π	PI

Super and subscripts

a, b, c	phase A, B, C

m	infinitesimal conductor
cal	calculation value
max	maximum value
n	specific moment

1 Introduction

Overhead lines are a common and economical way of power transmission, which can efficiently utilize space resources, reduce land occupation, and achieve long-distance power transmission. However, in the actual operation of the lines, they are often affected by natural conditions, which would result in faults and thus cause power supply interruption and economic losses. In order to improve the safety and stability of overhead line operation, large-scale monitoring equipment is needed to monitor various parameters of overhead lines and determine the line operation status [1]. Due to the long-term operation of the lines and gravity, the sag of overhead lines will aggravate, which increases the possibility of line short circuits. The methods for monitoring line sag include remote sensor measurement, optical measurement, image processing, *etc*. [2,3]. Considering the safety and convenience of staff for equipment operation and maintenance, the current advanced remote and non-contact measurement technology based on electromagnetic field (EMF) sensors can greatly compensate for some shortcomings of previous monitoring methods, such as difficulty in deploying on a large scale, high monitoring cost, *etc*.

Non-contact measurement technology for overhead line monitoring based on EMF sensing includes electric field measurement and magnetic field measurement. The idea of using the electric field to measure line sag is based on the potential difference, *i.e.*, voltage, between the line and a point in space. Then, establishing the relationship between voltage and electric field and predicting sag through electric field measurement and inverse algorithm [4]. Since the voltage of the line is almost constant, it can be assumed that the sag is only related to the spatial position of the conductor. Based on the above principle, Mukherjee *et al.* [5] measured the potential magnitude and relative phase of multiple points in space to calculate the line sag and developed a high-sensitivity measurement system on account of the phase difference of spatial potential at multiple points. Ji and Yuan [6] established a mathematical model of the overhead line and measurement point based on the electromagnetic induction principle and calculated the sag and voltage of any line only according to the position of the measurement point and measured spatial potential. Zhu *et al.* [7] used a capacitance coupling method to establish the impedance relationship between the voltage of the overhead line and voltage on the induction bar, from which the voltage of the three-phase line and location of the line are inversely calculated. Chen *et al.* [8] successfully calculated the voltage frequency of overhead lines by utilizing an electric field sensor and combining it with a frequency inversion algorithm. Xiao *et al.* [9] considered the influence of ambient wind on the line, the mathematical model of the electric field of the line, and the accuracy of the voltage calculation of the overhead line was improved. In summary, it is often only possible to invert some of the electrical parameters of an overhead line by directly measuring the electric field underneath the line; if the line sag is to be calculated, an induction bar needs to be placed underneath the line to rederive the mathematical model based on the principle of electromagnetic induction, which makes the calculation more complicated. In contrast, establishing a mathematical model of the magnetic field of an overhead line is simpler; the analytical solution of the magnetic field of the line has been sufficiently researched [10–12]. However, magnetic field measurement requires high-sensitivity magnetic field sensors and enhanced anti-interference ability of measurement elements. Fortunately, since the discovery of the Hall magnetoresistance effect, various magnetoresistance effects with higher magnetoresistance ratios have emerged, such as anisotropic magnetoresistance [13], giant magnetoresistance [14], extraordinary magnetoresistance [15], and tunneling magnetoresistance (TMR) [16] brought by the development of spintronics [17], which have higher measurement resolution than other types of magnetic sensors by two orders of magnitude [18]. These new sensors make it possible to directly measure magnetic field under overhead lines. Among them, TMR sensors are especially suitable for magnetic field measurement of overhead lines. In recent years, many scholars have used magnetic sensors to calculate overhead line sag and current. To obtain strong magnetic field signals and enhance anti-interference ability, magnetic sensors can be considered to be deployed on the tower. Khawaja *et al.* [19] deployed three dual-axis TMR sensors on the top of the tower to detect the line magnetic field and proposed an algorithm to calculate the current and sag of each phase line. Subsequently, Khawaja and Huang [20] further considered the line galloping, combined with a GPS to obtain the sag of each phase line when there is a swing. After establishing the mathematical model of the sensor and line, the sag, galloping, and current of the overhead line can be calculated with iterative calculation. However, magnetic sensors deployed on the tower will cause trouble for maintenance. Wu *et al.* [21] combined a TMR magnetic sensor with a UAV and proposed a reconstruction algorithm combining meta-heuristic and traditional optimization methods to calculate the current and sag of

overhead transmission lines by sampling magnetic field information at various positions below the lines. In addition, magnetic sensors can also be deployed on the ground. Xu *et al.* [22] deployed five two-axis TMR magnetic sensors on the ground, which not only considered the current and sag of the overhead line but also the calculation of tower tilt. However, deploying a magnetic sensor array on the ground will be limited by terrain; only vertical sensor array can avoid it. Chen [23] used a vertically arranged three-axis TMR sensor array to measure the magnetic field of a three-phase overhead line and calculate line current. Although the topographic effect can be overcome, it does not consider the sag of the line. The current literature research focuses mainly on how to deploy magnetic sensors simply and conveniently (as convenient as possible for management), how to enhance the anti-interference ability of magnetic sensors (especially in the application background of overhead lines), whether magnetic sensors can be deployed on a large scale (involving cost and power consumption of measurement system), *etc*. There is still no scheme for easy deployment of magnetic sensors considering the sag of the three-phase overhead line and no corresponding algorithm for reconstructing the three-phase overhead line current and sag.

Based on the first problem above, this article presents a parameter to evaluate the placement of the sensor, considering the dual influence of the magnetic field and mathematical model. For the second problem, this article presents a method to measure the sag and current of three-phase overhead lines. The method proposed in this article uses a TMR sensor array to measure the magnetic field of overhead lines. The TMR sensor array can overcome the adverse effects of terrain and is easy to install. In addition, the sensor array combined with the established current-sag inversion algorithm can accurately calculate the sag of the line, the instantaneous value of different types of current, the amplitude, and the phase angle. Because the magnetic field of the line is not affected by the natural environment, and the TMR sensor has low cost and low power consumption, the TMR sensor array proposed in this article is suitable for large-scale deployment and easy management.

The main contents of this article are as follows: Section 2 describes the theoretical and simplified model of EMF of the three-phase overhead line and compares the magnetic field error of the three-phase line calculated with the two models. Section 3, the type of TMR sensor is determined according to the established mathematical model, and the influence of the magnetic field and mathematical model on the placement of the sensor is analyzed. In Section 4, the structure of the TMR sensor array and current-sag inversion algorithm are introduced, and a typical three-phase overhead line is selected to verify and analyze the proposed sensor array and algorithm.

2 Current-sag prediction model

2.1 Theoretical model of EMF for three-phase overhead lines

Bundled conductors are often used in overhead lines to reduce the electric field strength at the surface of the conductor and to limit the generation of corona. These conductors are fixed by spacer bars, which can be treated as a single transmission line of the same length and the same sag, considering the long transmission distance of the overhead line and the small sag relative to the overall height of the transmission line [24]. Figure 1(a) shows a schematic diagram of a 500 kV three-phase overhead line and a TMR sensor array. The overhead lines are, from left to right, phase A, phase B, and phase C. The distance from the lines' suspension point to the ground is H, and the span of the lines is L. It should be noted that the suspension heights of the same-phase line are the same. The sag of phase A is marked as sag_A in the figure. In addition, a TMR sensor group composed of N vertically placed TMR sensors is installed below the line, and the vertical spacing of TMR sensors is d. The TMR sensor group is mounted on a detection rod, which is placed on the ground and has a horizontal spacing of p between neighboring detection rods. The TMR sensor array consists of these detection rods, and the jth sensor of each detection rod collectively constitutes the jth layer of sensors, *e.g.*, $T1 - S1$, $T2 - S1$, and $T3 - S1$ collectively constitute the first layer of sensors. Figure 1(b) shows the schematic structure of the yz section where the suspension point of the 500 kV three-phase overhead line is located. The spacing between the phases of the line is 13.2 m. The suspension height of phase A and phase C is 22 m, and the suspension point of phase B is 2.35 m away from the suspension point of phase C. The sag of each phase in the figure is sag_A, sag_B, and sag_C, in turn. As shown in Figure 1(a), the geometrical shape formed by the overhead conductor under the action of both temperature and gravity can be described by using the catenary line equation. This equation requires that the suspension heights of the same-phase line are the same, as shown in the following equation:

$$z = H + \alpha\left[\cosh\left(\frac{x}{\alpha}\right) - \cosh\left(\frac{L}{2\alpha}\right)\right], \quad -\frac{L}{2} < x < \frac{L}{2} \tag{1}$$

where α is the coefficient of the catenary line, H is the suspended height of the overhead line, and L is the span.

In order to calculate the magnetic field generated by overhead lines, it is considered that in steady-state

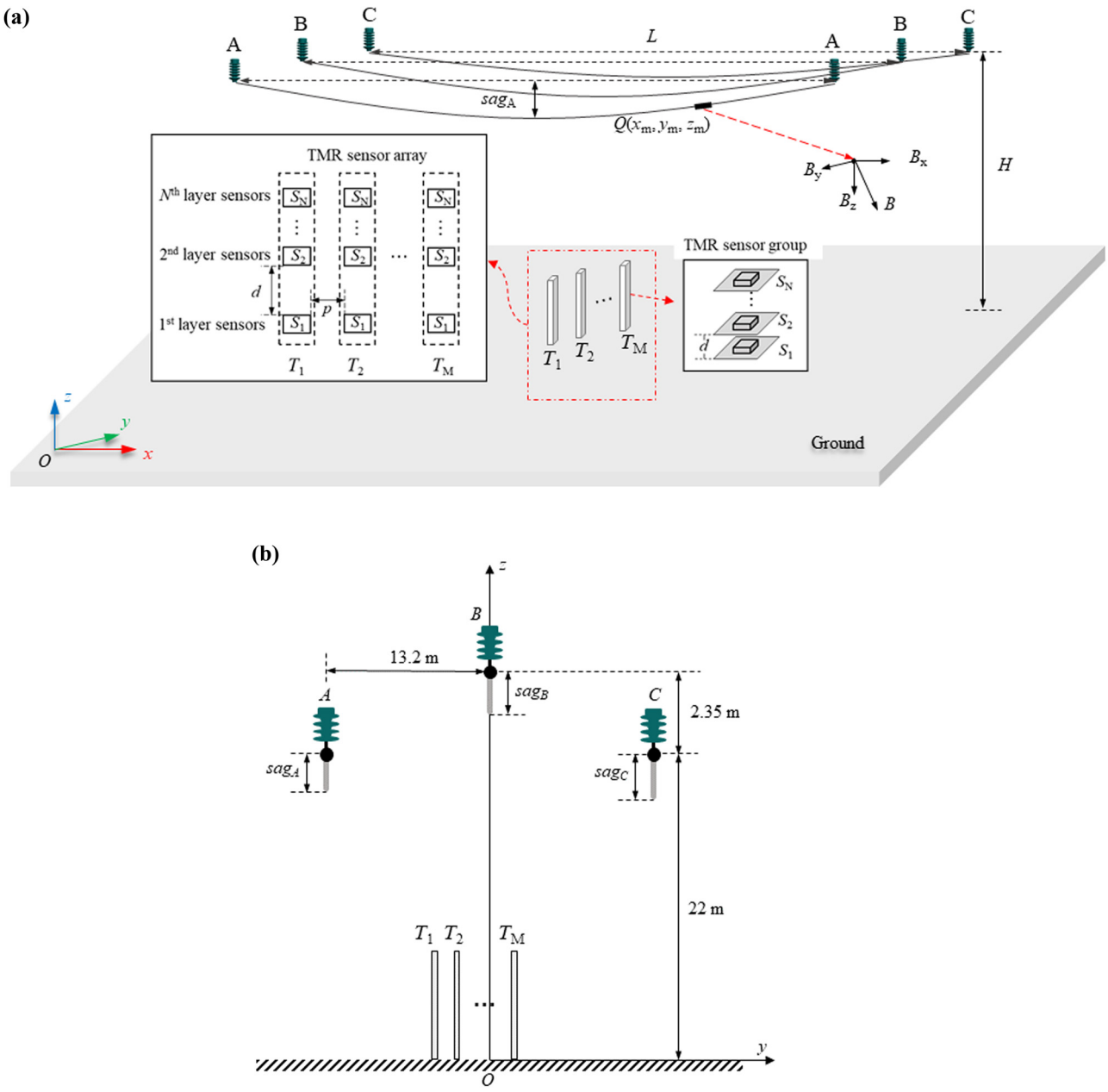

Figure 1. The: 500 kV three-phase overhead line model (ignoring tower): (a) diagram of three-phase overhead line and sensor array, and (b) *yz* section structure diagram of suspension point of three-phase overhead line.

electromagnetism, the strength of the magnetic field excited by a charged infinitesimal conductor at any point in space can be derived from the Biot–Savart law. Note that in the overhead transmission line system, the EMF excited by the transmission line is generally a low-frequency EMF [25], and the wavelength of the electromagnetic wave is much larger than the characteristic scale of the conductor, so it can be approximated as a quasi-stationary EMF, and thus the Biot–-Savart law can be applied to calculate the magnetic field strength excited by the overhead transmission line at an arbitrary point in the space as shown in the following equation:

$$\overrightarrow{B} = \frac{\mu_0}{4\pi}\int_1 \frac{Id\overrightarrow{l} \times \overrightarrow{r}}{r^3}, \tag{2}$$

where μ_0 is the vacuum permeability, I is the current of the infinitesimal conductor, l is the integral path along the curve where the conductor is located, and $\overrightarrow{r}$ is the position vector of the infinitesimal conductor to the field point.

As shown in Figure 1(a), combining Eqs. (1) and (2) yields the magnitude of the absolute value of the magnetic field strength excited by any infinitesimal conductor Q (x_m, y_m, z_m), where x_m, y_m, and z_m represent the coordinates of infinitesimal conductor, on a single overhead line at the spatial point P (x, y, z), as in the following equations:

$$B = \sqrt{B_x^2 + B_y^2 + B_z^2}, \tag{3}$$

$$B_x = \frac{\mu_0 I}{4\pi} \int_{-\frac{L}{2}}^{\frac{L}{2}} \frac{\sinh(x_m/\alpha)(y_m - y)dx_m}{r^3}, \tag{4}$$

$$B_y = \frac{\mu_0 I}{4\pi} \int_{-\frac{L}{2}}^{\frac{L}{2}} \left[\frac{\sinh(x_m/\alpha)(x - x_m)}{r^3} - \frac{(z - z_m)}{r^3} \right] dx_m, \tag{5}$$

$$B_z = \frac{\mu_0 I}{4\pi} \int_{-\frac{L}{2}}^{\frac{L}{2}} \frac{(y - y_m)dx_m}{r^3}, \tag{6}$$

$$r = \sqrt{(x - x_m)^2 + (y - y_m)^2 + (z - z_m)^2}, \tag{7}$$

where B_x, B_y, and B_z are the components of the magnetic field strength in the x, y, and z axes, respectively; and I is the current of a single overhead conductor.

For n overhead transmission lines, the magnetic field excited by each line interacts with each other, and the principle of vector superposition can be applied to write the magnitude of the absolute value of the magnetic field strength excited by multiple overhead transmission lines at the same point in space. Here, only the magnetic field components in each direction are considered in the following equations:

$$B_x = \sum_{i=1}^{n} I_i C_i^x, \tag{8}$$

$$B_y = \sum_{i=1}^{n} I_i C_i^y, \tag{9}$$

$$B_z = \sum_{i=1}^{n} I_i C_i^z, \tag{10}$$

where

$$C_i^x = \frac{\mu_0}{4\pi} \int_{-\frac{L}{2}}^{\frac{L}{2}} \frac{\sinh(x_m^i/\alpha)(y_m^i - y)dx_m}{r_i^3}, \tag{11}$$

$$C_i^y = \frac{\mu_0}{4\pi} \int_{-\frac{L}{2}}^{\frac{L}{2}} \left[\frac{\sinh(x_m^i/\alpha)(x - x_m^i)}{r_i^3} - \frac{(z - z_m^i)}{r_i^3} \right] dx_m, \tag{12}$$

$$C_i^z = \frac{\mu_0}{4\pi} \int_{-\frac{L}{2}}^{\frac{L}{2}} \frac{(y - y_m^i)dx_m}{r_i^3}. \tag{13}$$

Considering that the physical model in this article is a three-phase overhead transmission line and multiple magnetic sensors (S_1, S_2, S_3, ..., S_N) are required to measure the magnetic field strength under the overhead line, the magnitude of the magnetic field strength at the location of each sensor needs to be calculated simultaneously. To facilitate the calculation, the coordinates of each sensor are noted as S_j (x_j, y_j, z_j), and the coordinates of the sensors are substituted into Eqs. (11)–(13), whereby Eqs. (8)–(10) are organized into a generalized matrix form as follows:

$$\overrightarrow{B_\xi} = G_\xi \vec{I}, \tag{14}$$

where

$$\overrightarrow{B_\xi} = [B_{S_1}^\xi \quad B_{S_2}^\xi \quad \cdots \quad B_{S_N}^\xi]^T, \tag{15}$$

$$G_\xi = \begin{bmatrix} C_{11}^\xi & C_{21}^\xi & C_{31}^\xi \\ C_{12}^\xi & C_{22}^\xi & C_{32}^\xi \\ \vdots & \vdots & \vdots \\ C_{1N}^\xi & C_{2N}^\xi & C_{3N}^\xi \end{bmatrix}, \tag{16}$$

$$\vec{I} = [I_1 \quad I_2 \quad I_3]^T, \tag{17}$$

where ξ takes x, y, and z, depending on the magnetic field strength components in the direction to be calculated. The first subscript of the variable C represents the number of the conductor, and the second subscript represents the number of the sensor. Since the variable C contains only the geometric position information of the overhead conductor and the sensor, the matrix $\boldsymbol{G}_\xi$ is called the position matrix. Once the position matrix $\boldsymbol{G}_\xi$ is determined, the current of each conductor can be calculated.

According to the theoretical model of the electro-magnetic field of the overhead line established in the previous paper, EMF calculation is carried out for the 500 kV three-phase overhead line [26] shown in Figure 1(b). The geometrical parameters of the line are shown in Figure 1(b), taking the span of the line L = 400 m. Other parameters are shown in Table 1. The influence of the current in the other line spans has been analyzed in the literature [27], which shows that only the effect of the neighboring lines needs to be considered. The magnetic field strengths at the locations of vertical heights z = 0 m, z = 2 m, and z = 4 m are calculated, respectively, and the results are shown in Figure 2. Figure 2(a) shows the distribution of magnetic field strength (B) in the xy plane directly under the overhead line. As can be seen from the figure, the magnetic field strength (B) is strongest at the position where the

Table 1: Calculation conditions for EMF at one instant of time

Phase	Current (A)	Sag (m)
Phase A	1,000	8
Phase B	−500	8
Phase C	−500	8

center of the *xy* plane deviates a short distance from the negative direction of the *y*-axis. Since the current in phase A is the largest, the maximum value of the magnetic field strength after superposition should be located below phase A. Within the spacing range of the line $y \in (-13.2\ \text{m}, 13.2\ \text{m})$, the magnetic field strength (B) is greater than that at other locations outside the spacing, and the magnetic field strength within the spacing increases significantly with height. The elliptical distribution of the magnetic field strength is caused by the fact that the span of the overhead line is larger than the spacing of each phase of the line. Figure 2(b)–(d) shows the distribution of magnetic field strength components B_x, B_y, and B_z in the *xy* plane at different heights. In Figure 2(b), the magnetic field strength component $B_x = 0$ T at $x = 0$ m, and therefore, the value of B_x cannot be measured at that location; in Figure 2(c), the range $y \in (-5\ \text{m}, 0\ \text{m})$ spans $B_y = 0$ T, and therefore, the value of B_y cannot be measured at some locations in this range either; and in Figure 2(d), the locations spanning $B_z = 0$ T are located outside of the line spacing. Therefore, the B_z value can be measured in the line spacing range $y \in (-13.2\ \text{m}, 13.2\ \text{m})$.

2.2 Simplified model of EMF for three-phase overhead lines

For the theoretical model, multiple numerical integrations (Eqs. (11)–(13)) are required to calculate the variable C, which increases the computational complexity of current and sag reconstruction, so a simplified EMF model can be considered to compute the variable C. Budnik and Machczyński [27] assume that the magnetic field generated at a

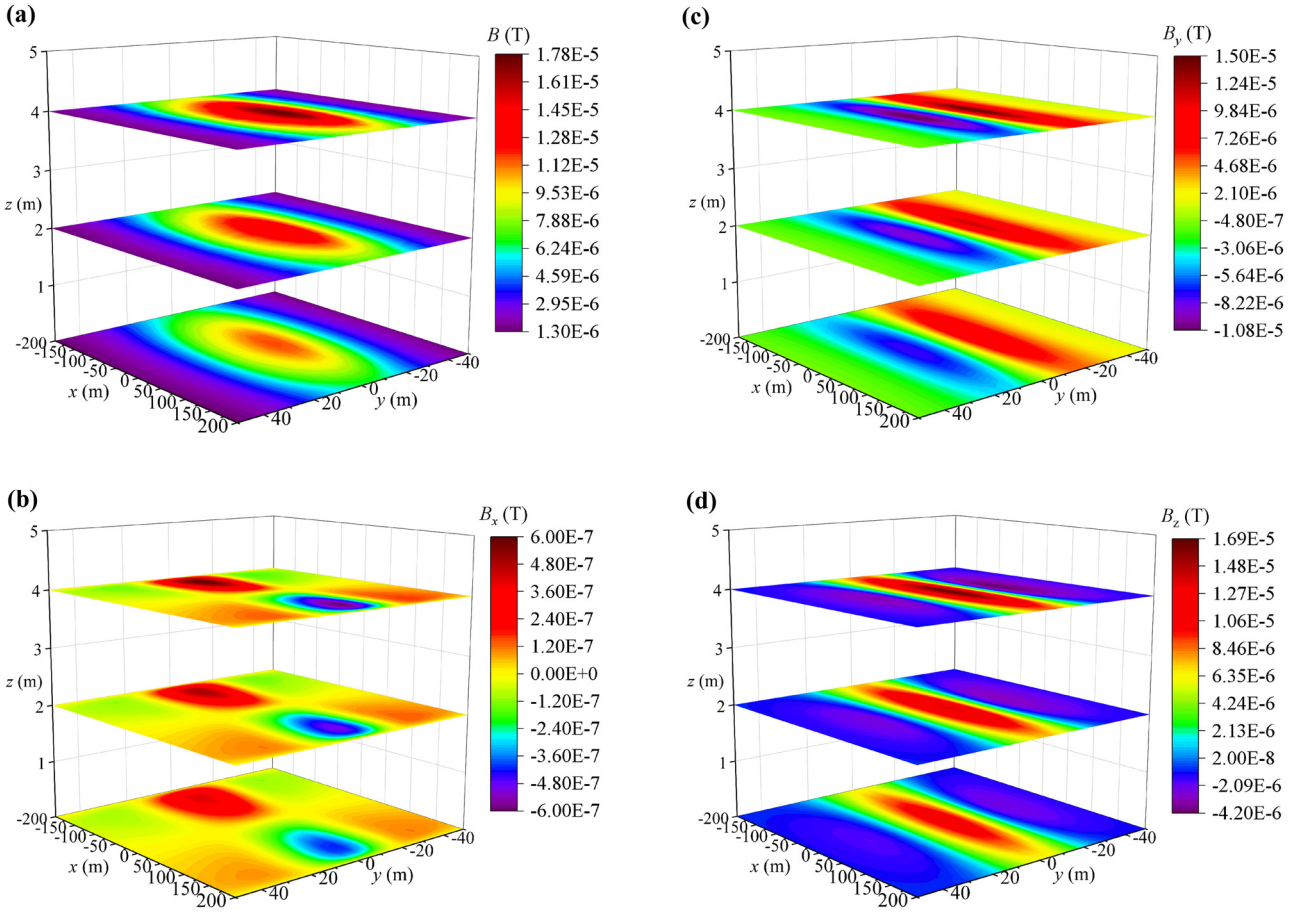

Figure 2: Magnitude of the magnetic field strength and its components calculated by the theoretical model: (a) B, (b) B_x, (c) B_y, and (d) B_z.

point on an overhead conductor is generated by an infinitely long straight conductor of the same height (the height of the point can be calculated by Eq. (1)). Therefore, the magnitude of the magnetic field and its components for each phase can be computed directly from Ampere's law:

$$B = \frac{\mu_0 I}{2\pi r}. \tag{18}$$

Budnik and Machczyński [27] used the above-simplified model to calculate the magnetic field of an infinitely long conductor located at the height of the sag and at the height of the suspension point, respectively, and compared it with the theoretical model. The results show that the error between the simplified model and the theoretical model in calculating the magnetic field at the mid-point of the line is about 0.05–0.2%, and at the suspension point, the error is about 3–4%. Note that when calculating the superimposed magnetic field of each conductor in this article, only the calculation of variable C needs to be modified. Since it is assumed that each phase conductor is composed of multiple infinite long straight conductors along the x-direction, the component of the magnetic field in the x-direction is 0. The variable C is calculated as follows:

$$C_i^x = 0, \tag{19}$$

$$C_i^y = \frac{\mu_0}{2\pi}\frac{z_{\mathrm{m}}^i - z}{r_i^2}, \tag{20}$$

$$C_i^z = \frac{\mu_0}{2\pi}\frac{y - y_{\mathrm{m}}^i}{r_i^2}. \tag{21}$$

In order to quantify the error between the simplified model and the theoretical model of the EMF, the magnetic field intensity at the height z = 0 m, z = 2 m, and z = 4 m is calculated with the simplified model in the xy plane (the calculation conditions are the same as those in Section 2.1). The relative error of the magnetic field intensity between the simplified model and the theoretical model is shown in Figure 3. As can be seen in Figure 3(a), the relative error of the magnetic field intensity calculated by the simplified model and the theoretical model in the x range of [−150 m, 150 m] is δ < 0.75% at different height planes, whereas near the suspension point, the error grows rapidly to more than 6%. Figure 3(b) shows that in the y = 0 m plane, the relative error δ < 0.4% between the simplified model and the theoretical model along the x direction. The above results show that using the simplified model to solve the magnetic field inverse problem can not only maintain high calculation accuracy but also greatly reduce the calculation complexity.

3 TMR sensor selection and placement analysis

TMR sensors can be categorized into single-axis, dual-axis, and tri-axis magnetic sensors according to the direction of the sensitive axis. When performing magnetic field measurements and current calculations for overhead lines, using different types of TMR sensors will cause the matrix (Eq. (16)) to change, which will affect the placement of different types of sensors. It can be recalled that some literature on the calculation of overhead line current inverse problems [23,28] use the condition number of the position coefficient matrix to determine the reasonable placement location of the selected sensors. The condition number (Eq. (22)) reflects, to some extent, the degree of

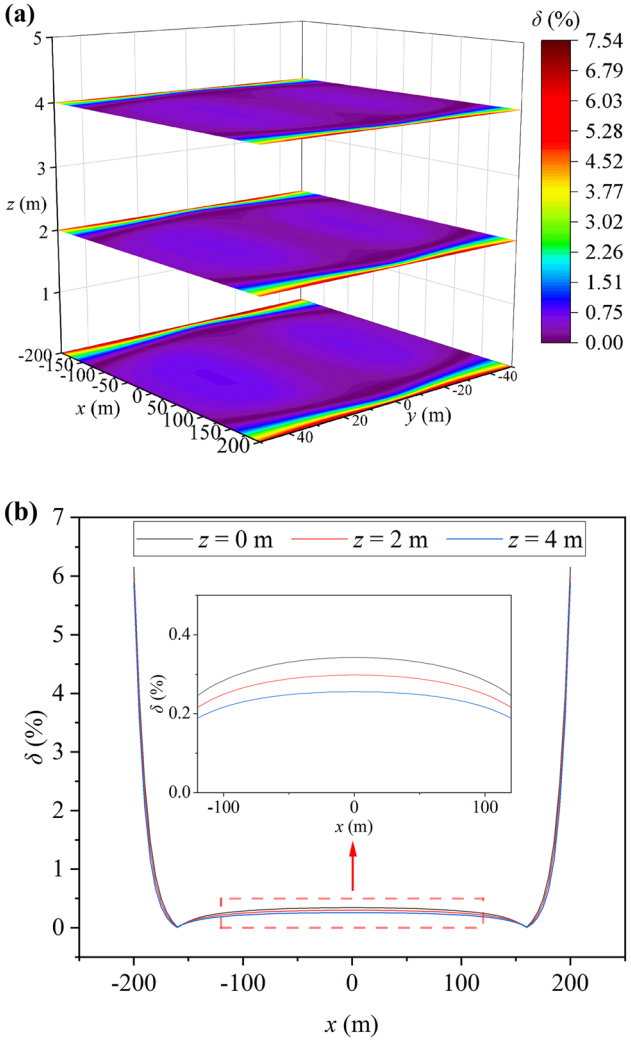

Figure 3: Relative errors between simplified and theoretical models of magnetic field: (a) xy planes of different heights and (b) y = 0 m plane.

perturbations in the equations on the solution of the equations

$$\frac{\|\Delta I\|}{\|I\|} \le \|G\|\|G^{-1}\|\cdot\left(\frac{\|\Delta B\|}{\|B\|}+\frac{\|\Delta G\|}{\|G\|}\right), \tag{22}$$

where $\mathrm{Cond}(G) \triangleq \|G\|\cdot\|G^{-1}\|$ is the condition number of matrix G.

When the condition number is too large, the mathematical model established is ill-posed. If the established model is nonlinear, it will lead to the amplification of errors in the solving process, and the calculation results will completely deviate from the real value. Therefore, in order to maintain the stability and accuracy of the mathematical model of the inverse problem, it is necessary to consider the size of the condition number of the mathematical model matrix based on different types of sensors in different installation locations.

3.1 Effect of condition number on TMR sensor array placement

First, consider the condition number of the simplified model built from a single-axis TMR sensor array. To be clear:

(1). The calculations do not involve EMF. The sag values of each phase line are shown in Table 1. The horizontal distance p between sensors is 1 m.

(2). When using the simplified model to calculate the magnetic field, there is no x-axis magnetic component, so there is no need to calculate the matrix condition number of the x-axis sensor.

(3). Three single-axis TMR magnetic sensors located in the xy plane are used for the calculation (*i.e.*, the first sensors of each group in Figure1(a): $T_1 - S_1$, $T_2 - S_1$, and $T_3 - S_1$), and the line where the sensors are located is parallel to the y-axis.

(4). In order to shorten the calculation time, the step length $\Delta x = \Delta y = 5$ m is taken when calculating the condition number.

The condition numbers of the matrices G_y and G_z calculated at the $z = 0$ m plane, respectively, are shown in Figure 4, and the calculated condition numbers are converted to logarithm with base 10. As can be seen from this figure, the condition number of G_y is minimal at $y = 0$ m along the x coordinate in the range of the line's span, and the condition number of G_z has two valley regions, in the positive half-axis valley region of the y-axis, the condition number is minimal at $y = -5$ m; in the negative half-axis valley region of the y-axis, the condition number is minimal

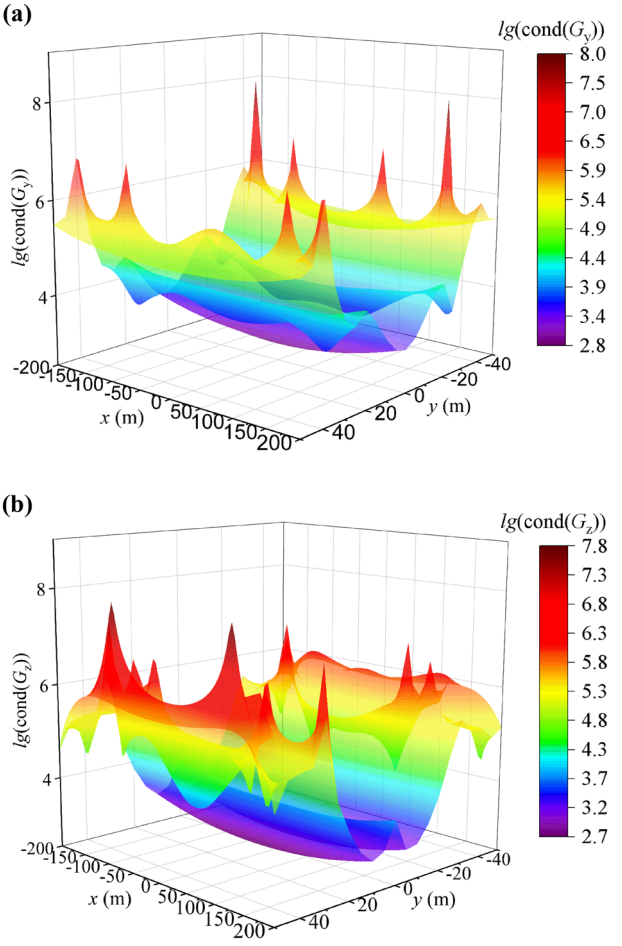

Figure 4: The condition numbers of the three single-axis sensor coefficient matrices obtained by the simplified EMF model at $z = 0$ m: (a) G_y and (b) G_z.

at $y = 10$ m. On the xy plane at $z = 0$ m, the condition number of G_y takes the minimum value of about 721 at (0, 0); the condition number of G_z takes the minimum value of about 535 at (0, −5), and the condition number at (0, 10) is about 549. According to the calculation results of the condition numbers of matrices G_y and G_z, when using a single-axis TMR magnetic sensor, if it is required that $\lg(\mathrm{cond}(G)) < 3.3$ for matrices G_y and G_z, then the reasonable placement area of the y-axis sensor is $\{(x, y) \mid x \in (-200, 200), y \in (-5, 5)\}$, and the reasonable placement area of the z-axis sensor is $\{(x, y) \mid x \in (-200, 200), y \in (-10, 0) \cup (0, 10)\}$.

From the above calculation results of condition number, it can be found that the reasonable placement positions of the y-axis and z-axis sensors have some overlaps. Therefore, it is possible to consider using a dual-axis magnetic sensor at the overlapping area to obtain as much magnetic field information as possible and improve the mathematical model. Using the same sag values of each phase line in Table 1, the condition numbers of the coefficient matrix G_{yz}

constructed with the dual-axis magnetic sensor on the *xy* plane at different heights are calculated, and the calculation results are shown in Figure 5. As can be seen from the figure, at different heights, the condition number distribution of matrix G_{yz} is bag-shaped, reaching the minimum value at the line sag point, which is about 44, 33, and 25, respectively. In the area of $y \in (-15\text{ m}, 15\text{ m})$, the condition number of the dual-axis sensor coefficient matrix can be maintained at a relatively low level.

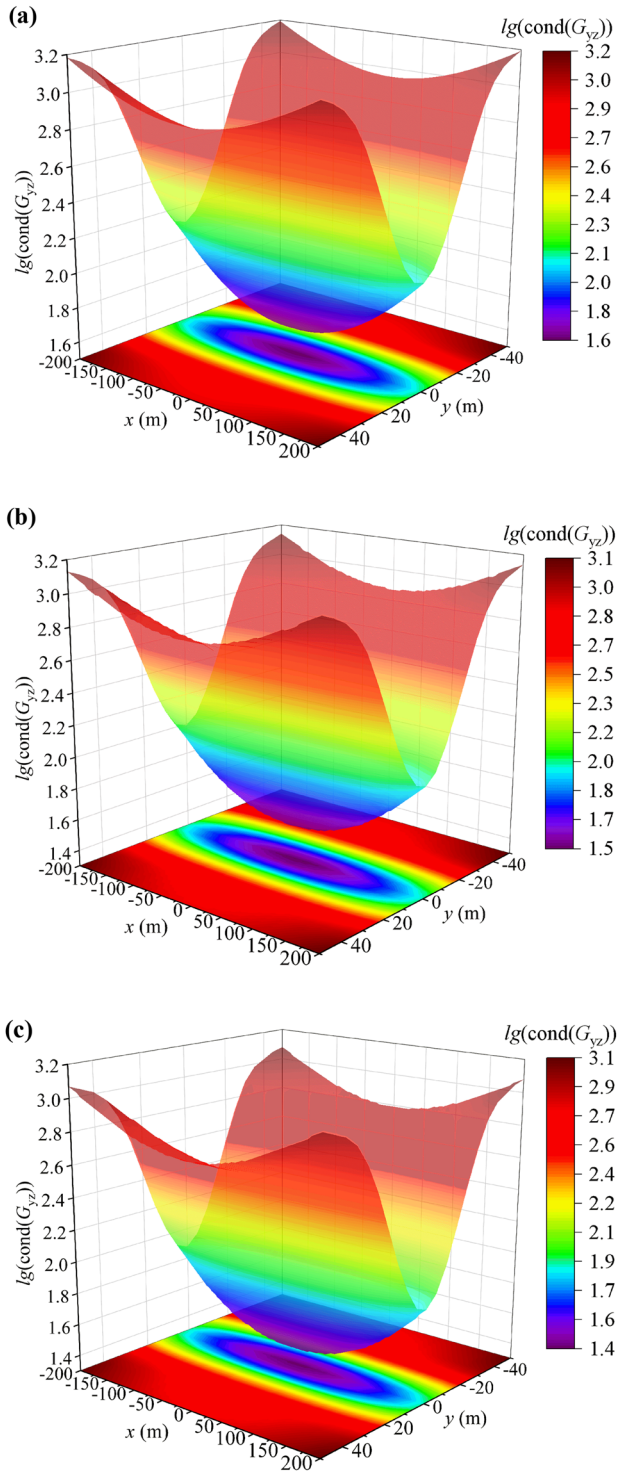

Figure 5: The condition numbers of the three dual-axis sensor coefficient matrices G_{yz} obtained by the simplified EMF model on the *xy* plane at different heights: (a) z = 0 m, (b) z = 2 m, and (c) z = 4 m.

3.2 Dual effects of magnetic field and condition number on TMR sensor array placement

By analyzing the condition number, the type and placement location of the TMR sensor can be basically determined. However, the condition number only affects the numerical calculation error, and it is also necessary to consider whether the sensor can obtain a sufficiently strong signal in the actual application process, which is the premise for subsequent calculations. At present, there is still no evaluation parameter for the sensor placement location under both influences of magnetic field and condition number in the literature. Therefore, this article defines the following sensor position sensitivity value (Eq. (23)) to evaluate the pros and cons of the sensor array placement location under both influences of magnetic field and condition number

$$\mathrm{ps}_\xi = \frac{1}{|B_{\xi,\ \max}| \cdot \mathrm{cond}(G)} \sum_i |B_{\xi,i}|, \tag{23}$$

$$\mathrm{ps} = \sum_\xi \mathrm{ps}_\xi, \tag{24}$$

where cond(G) is the condition number of the matrix formed by the sensor array. If it is the y-axis sensor array, then it is cond(G_y). If it is the yz-axis sensor array, then it is cond(G_{yz}); $B_{\xi,i}$ is the ξ-direction magnetic field intensity component measured by the ith sensor; $B_{\xi,\max}$ is the maximum ξ-direction magnetic field intensity component measured by the sensor array; ξ takes x, y, and z. ps_ξ represents the ratio of the relative size of the magnetic field measured by a certain type of sensor in a certain sensor array to the condition number of that sensor array, which is a parameter to evaluate the pros and cons of the placement location of a single sensor in the sensor array. ps is a parameter to evaluate the pros and cons of the placement location of the entire sensor array. The larger the ps value, the stronger the magnetic field signal measured by the sensor, and the more stable the mathematical model corresponding to the placement location. It is worth noting that the condition number cond(G) ≥ 1, so dividing the magnetic field value by the condition number is equivalent to shrinking the measured magnetic field value, and the physical meaning of the

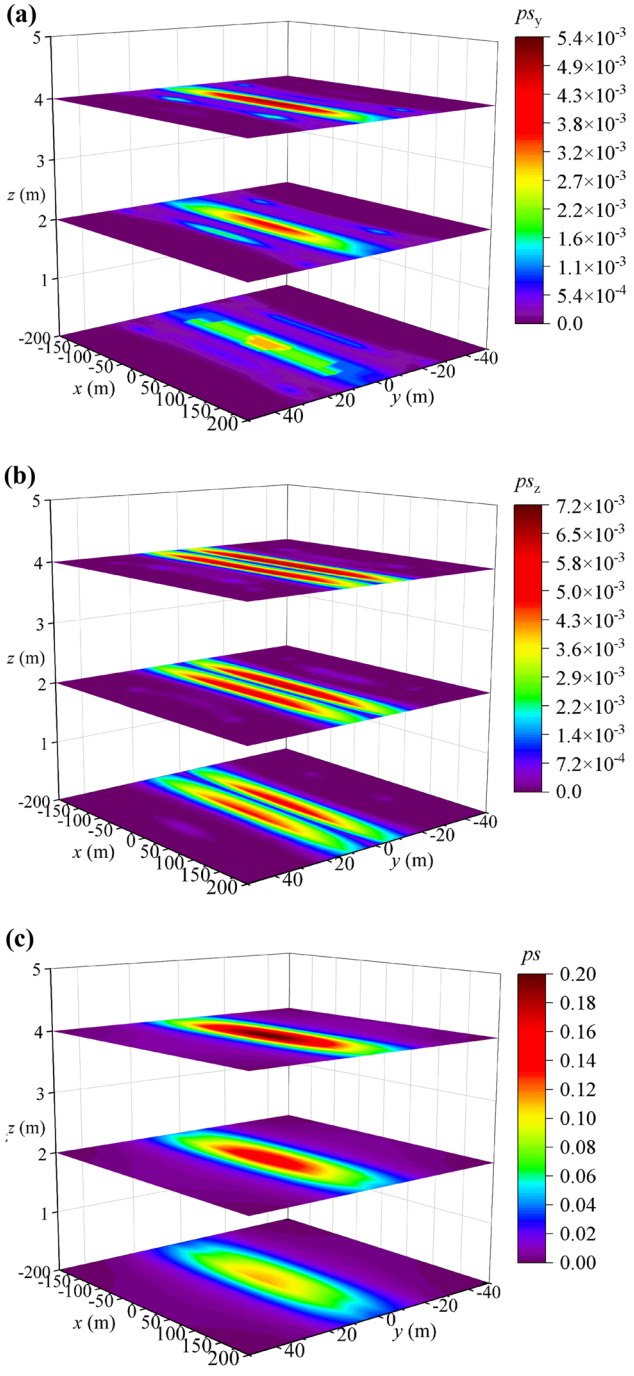

Figure 6: The position sensitivity values of the single-axis sensor array and the dual-axis sensor array obtained by the simplified EMF model on the *xy* plane at different heights: (a) ps_y of the *y*-axis sensor array, (b) ps_z of the *z*-axis sensor array, and (c) ps of the *yz*-axis sensor array.

ps value can be understood as the magnetic field intensity measured by the sensor array after being affected by its established mathematical model. In order to evaluate the placement location of the entire sensor array, it is necessary to dimensionless and sum up the magnetic field values measured by each sensor in the sensor array, so as to evaluate whether most sensors in this sensor array can measure relatively strong magnetic field values at a certain location.

Next, the ps values of the single-axis sensor array and dual-axis sensor array are calculated using the simplified magnetic field model (the calculation conditions are shown in Table 1). The position sensitivity values of the single-axis sensor array and the dual-axis sensor array calculated by the simplified magnetic field model on the *xy* plane at different heights are shown in Figure 6. As shown in Figure 6(a), the calculation results of ps_y indicate that the reasonable placement area of the *y*-axis sensor array is $\{(x, y) \mid x \in (-25, 25), y \in (0, 5)\}$, where $ps_y > 2.7 \times 10^{-3}$ in this area. Since the influence of the magnetic field is considered, $\{(x, y) \mid x \in (-200, 200), y \in (-5, 5)\}$ (Figure 4(a)) is not the reasonable placement area for the *y*-axis sensor array anymore. In addition, as the height increases, not only does the ps_y value increase in the area, but also the reasonable placement area expands. Figure 6(b) shows that there are two areas suitable for arranging *z*-axis sensor arrays on the *xy* plane: $\{(x, y) \mid x \in (-125, 125), y \in (-13, -5) \cup y \in (3, 10)\}$. In these two areas, $ps_z > 3.6 \times 10^{-3}$. Figure 6(b) is similar to Figure 4(b) in terms of condition number distribution, and there exist two reasonable placement areas, which is because within the spacing range under the overhead line $y \in (-13.2\,\text{m}, 13.2\,\text{m})$, B_z is strong (as shown in Figure 2(d)), so the magnetic field value has little influence on ps calculation, and the sensor position sensitivity value is mainly affected by condition number at this time. As shown in Figure 6(c), for the position sensitivity value of the dual-axis sensor array (*yz*-axis sensor), its distribution on the *xy* plane is similar to that of the condition number in Figure 5. This is because the magnetic field in Eq. (24) is the sum of measurement results of each axis sensor, and since B_y is smaller than B_z within the spacing range under overhead line $y \in (-13.2\,\text{m}, 13.2\,\text{m})$, B_z occupies a larger proportion in Eq. (24). In addition, the condition number cond (G_{yz}) of the dual-axis sensor array in Eq. (24) is similar to B_z distribution, so under the dual effect of magnetic field and condition number, the position sensitivity value of the dual-axis sensor array is elliptical. The calculation results in Figure 6 show that the position sensitivity value of the dual-axis sensor array is significantly higher than that of the single-axis sensor array, so the dual-axis

Table 2: Parameters of the TMR sensor array

Number of detection rods (*M*)	Number of vertical sensors (*N*)	Sensor vertical space (*d* (m))
3	1	0
4	3	0.5

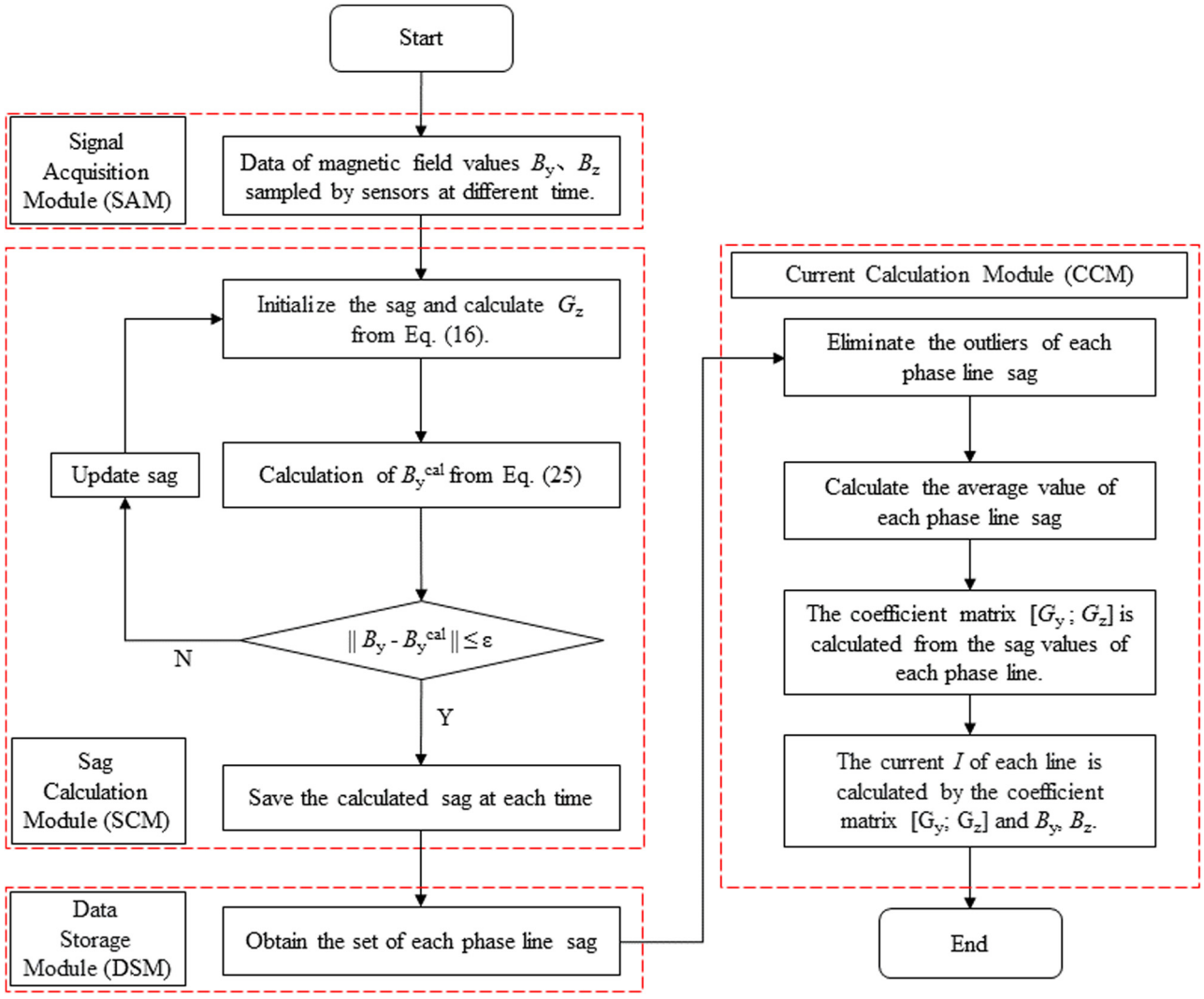

Figure 7: Current-sag inversion algorithm.

Table 3: Calculation results of line sag with balanced current

	Phase	Real value (m)	Calculated value (m)				Relative error (%)
			First layer	Second layer	Third layer	Mean	
Case 1	Phase A	8.0	8.13	8.06	8.13	8.11	1.33
	Phase B	8.0	8.02	8.00	7.98	8.00	0.00
	Phase C	8.0	8.18	8.21	8.13	8.17	2.18
Case 2	Phase A	7.4	7.56	7.53	7.44	7.51	1.48
	Phase B	7.8	7.87	7.82	7.78	7.82	0.26
	Phase C	7.2	7.38	7.40	7.22	7.33	1.87
Case 3	Phase A	9.6	9.78	9.78	9.63	9.73	1.35
	Phase B	9.1	9.09	9.09	9.09	9.09	−0.13
	Phase C	9.8	9.93	9.90	9.68	9.84	0.37

sensor array should be used for subsequent inverse problem calculations.

4 Current-sag inversion algorithm and verification

4.1 Current-sag inversion algorithm

Based on the analysis of the sensor array placement in Section 3, this article proposes a line current-sag inversion calculation algorithm. As previously mentioned, the suspension heights of the same phase line are the same. The TMR sensor array is placed at the midpoint (x = 0 m) of the overhead line span and on the ground within the line spacing range, as shown in Figure 1(b). Such placement has the following advantages:

(1) The magnetic field intensity at the midpoint of the line span (x = 0 m) is less affected by the neighboring lines, thus minimizing the magnetic field error measured by the sensors.
(2) According to the analysis in the previous section, the midpoint of the span is a position with both strong magnetic field intensity and a better mathematical model, thus reducing the error in the inversion calculation.
(3) The sensor array placed on the ground is not only easy to install but also faster and safer for subsequent inspection and maintenance.

When performing the inverse problem calculation of the mathematical model, the number of unknown parameters needs to be determined first, and then the specific parameters of the TMR sensor array are determined, including the number of sensors, the horizontal distance between adjacent detection rods, and the vertical distance between sensors on the same detection rod. This article considers the line current and sag, and there exist six unknown parameters: I_a, I_b, I_c, sag_A, sag_B, and sag_C. For this case, at least six equations are required for calculations. Because of using a dual-axis TMR sensor, one sensor can provide two independent equations, so three sensors can meet the minimum requirements. Thus, the specific parameters of the TMR sensor array under the minimum requirements can be determined, as shown in the first row of Table 2. The value of sensor horizontal spacing p is not given in the table. This value can be adjusted according to the sensor position sensitivity value. It is not required that the horizontal spacing between each detection rod be the same.

Note that the magnetic field intensity components measured by the dual-axis sensor can be approximated as the same point. According to Eq. (14), Eq. (25) can be obtained by eliminating the current value in the equation.

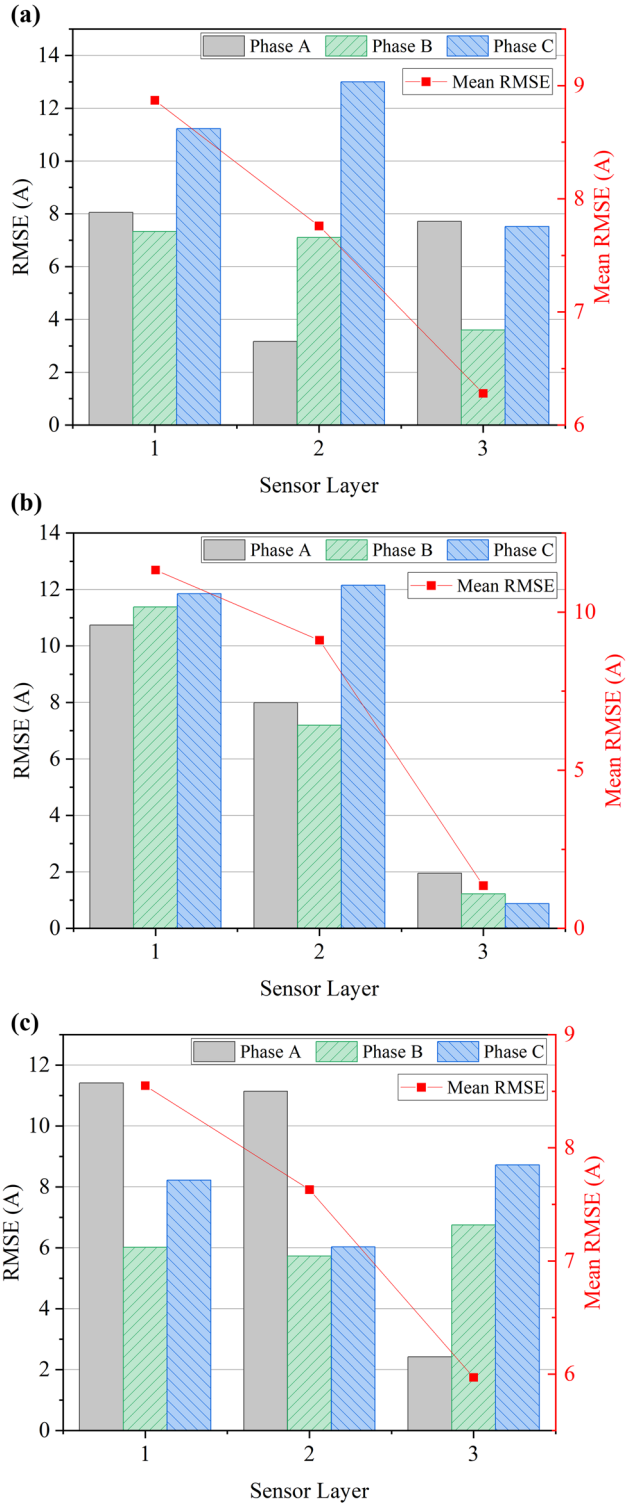

Figure 8: The RMSE and the mean RMSE calculated from each layer sensor in each case under balanced current: (a) Case 1, (b) Case 2, and (c) Case 3.

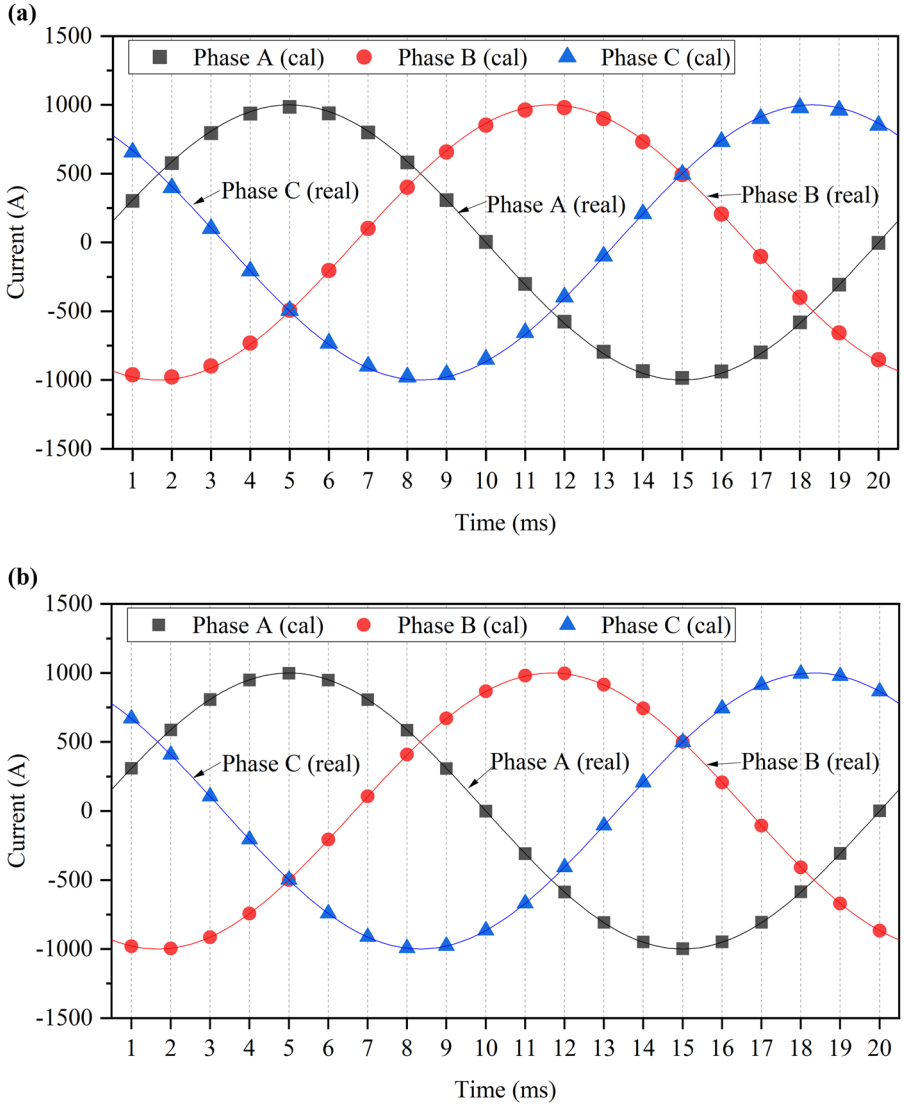

Figure 9: The calculated current of Case 2 in one cycle: (a) first layer and (b) third layer.

The equation represents a nonlinear equation group only related to three unknown sags. Thus, the sag can be calculated first, and then the current value of the line can be determined, thereby reducing the number of unknowns

$$B_y = G_y \cdot G_z^{-1} B_z, \tag{25}$$

$$\begin{cases} e = \|B_y - B_y^{\text{cal}}\| \\ \text{s.t. sag} \in S_{\text{set}}. \end{cases} \tag{26}$$

Eq. (26) is the mathematical model established in this article, where B_y is the measured magnetic field intensity in the y-direction; B_y^{cal} is the calculated magnetic field

Table 4: Calculated sag of Case 2 with 40 magnetic field values

	Phase	Real (m)	Calculated (m)				Relative error (%)
			First layer	Second layer	Third layer	Mean	
Case 2	Phase A	7.4	7.52	7.42	7.59	7.51	1.47
	Phase B	7.8	7.83	7.80	7.79	7.80	0.03
	Phase C	7.2	7.37	7.30	7.34	7.34	1.94

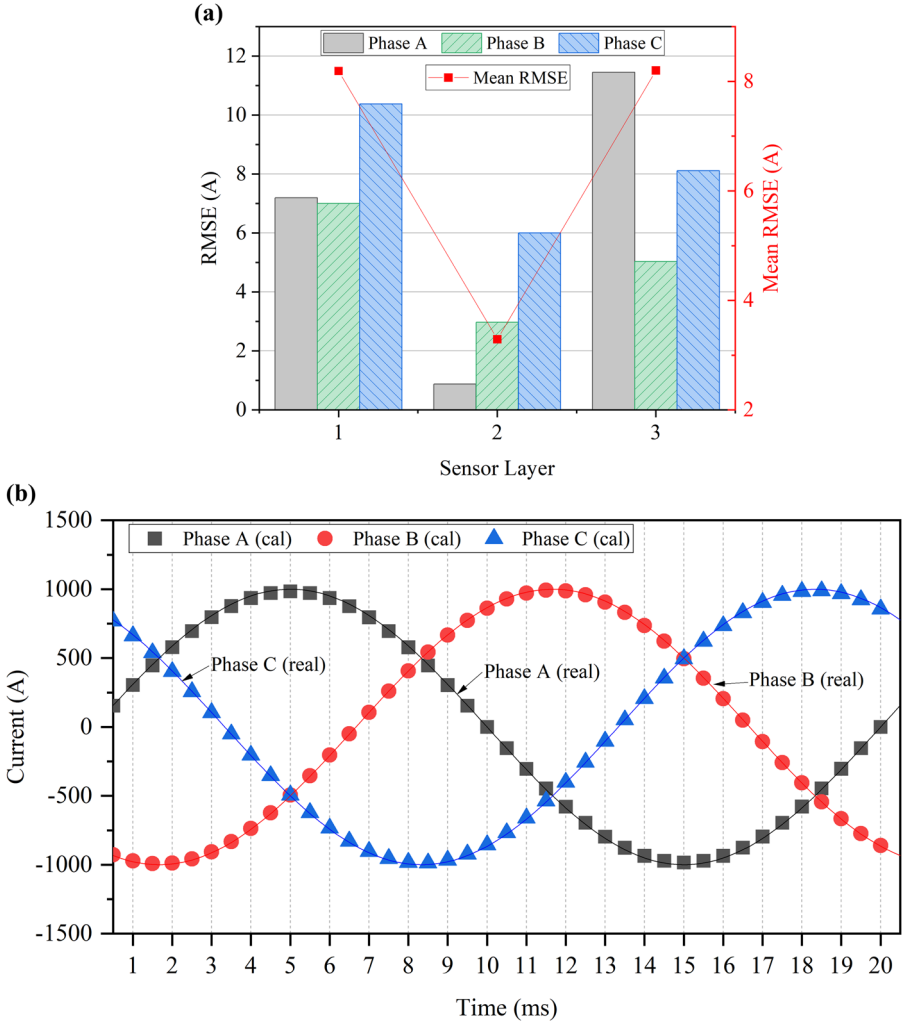

Figure 10: The calculated error from each layer sensor in Case 2 and the calculated current of maximum RMSE using 40 magnetic field values: (a) RMSE and mean RMSE of each layer sensor and (b) third layer in Case 2.

Table 5: Three kinds of unbalanced currents and their initial phases

	Phase	Current amplitude (A)	Initial phase (°)
Case 1	Phase A	800	30
	Phase B	700	−100
	Phase C	600	−190
Case 2	Phase A	750	−200
	Phase B	900	120
	Phase C	650	40
Case 3	Phase A	750	−60
	Phase B	600	100
	Phase C	850	140

intensity in the y-direction; e is the Euclidean distance between B_y and B_y^{cal}, which is also the target function used for the optimization; S_{set} is a manually set range of sag, where the variation of sag should be limited within S_{set}. Then, a current-sag inversion algorithm is proposed, as shown in Figure 7. The algorithm mainly includes four parts: signal acquisition module, sag calculation module (SCM), data storage module (DSM), and current calculation module (CCM). The calculation process of the algorithm is described as follows:

(1) Use sensors to sample B_y and B_z at each moment;
(2) Initialize the values of the three unknown sags; according to the collected magnetic field data B_y and B_z at the t_n moment, calculate the magnetic field component B_y at the t_n moment, that is, calculate the y-direction magnetic field intensity component with Eq. (25);
(3) Judge with Eq. (26) whether e satisfies the tolerance condition ε. If not, update the sags and repeat steps (2) and (3); if the tolerance condition is satisfied, store the sags at the current moment, turn to (1), and continue to calculate the sag value at the next moment t_{n+1};

Table 6: Calculation results of line sag with unbalanced current

	Phase	Real value (m)	Calculated value (m)				Relative error (%)
			First layer	Second layer	Third layer	Mean	
Case 1	Phase A	7.4	7.50	7.47	7.39	7.45	0.70
	Phase B	7.8	7.84	7.54	7.77	7.72	−1.09
	Phase C	7.2	7.44	7.43	7.38	7.42	3.01
Case 2	Phase A	7.4	7.64	7.64	7.66	7.65	3.34
	Phase B	7.8	7.71	7.70	7.69	7.70	−1.29
	Phase C	7.2	7.36	7.39	7.41	7.39	2.60
Case 3	Phase A	7.4	7.53	7.49	7.52	7.51	1.53
	Phase B	7.8	7.77	7.82	7.78	7.79	−0.13
	Phase C	7.2	7.43	7.40	7.45	7.43	3.18

(4) After finishing the calculation of the magnetic field B_y at all moments, obtain the sags at each moment and enter the CCM. Remove outliers in the line sag data set;
(5) Calculate the average sags of each phase line, that is, obtain the final sag value of each phase line;
(6) Merge the coefficient matrix to obtain $[G_y; G_z]$, and calculate the current value of each phase line at each moment according to the measured $[B_y; B_z]$.

In the SCM, nonlinear least squares (NLS) method is chosen for the calculation. In order to reduce the adverse effect of the least squares method falling into the local optimum, a random optimization algorithm is used to globally search for a better sag solution at first, and then further calculate it using NLS. Considering that the time spent on solving should be minimized as much as possible, it is more appropriate to use the surrogate optimization algorithm for global search. In the CCM, since the sag has been obtained, the linear system Eq. (14) can be solved directly to obtain the current value. The reason why the position coefficient matrix $\boldsymbol{G}_{\xi}$ is merged is that this can minimize the condition number of the matrix (as shown in Figure 6) and reduce the numerical calculation error. It should be pointed out that in the SCM, the sensors located in the same xy plane are selected for the calculation (such as $T_1 - S_1$, $T_2 - S_1$, $T_3 - S_1$), and the simplified model (Eqs. (19)–(21)) is used; in the CCM, all sensors are selected for the calculation, and the theoretical model (Eqs. (11)–(13)) is used to calculate the current value.

4.2 Verification and analysis of current-sag prediction method

To verify the rationality of the sensor placement position proposed in this article and the effectiveness of the algorithm, numerical calculations are carried out with MATLAB. The line parameters are shown in Figure 1(b). To improve the reliability of the calculation results, an array consisting of multiple vertical sensors is used. The parameters are shown in the second row of Table 2, where the first layer of sensors is located on the horizontal ground. The coordinates of the detection rods in the xy plane are as follows: T_1 (0, 7 m), T_2 (0, 6 m), T_3 (0, −6 m), T_4 (0, −7 m). If the number of sensor layers needs to be increased, the vertical spacing d of the sensors should be reduced.

First, the calculation and verification analysis of the balanced three-phase current under different sag is carried out. The sinusoidal current amplitude of the line is 1 kA, and the phases are 0, −120°, and 120°, respectively. In one current cycle, 20 magnetic field values are sampled with Δt = 1 ms, and the sag of each phase line is calculated based on these data points. The calculation results are shown in Table 3. The average sag in Table 3 is the average of the sag values calculated by the sensors of each layer, and the relative error is calculated by comparing the average sag with the real value. It can be seen that the relative error of the sag calculated with the algorithm proposed in this article is less than 3%. After calculating the sag, the DSM collects the sag values at each moment, and the CCM calculates the current values at each moment. For the case of balanced current in the line, the root mean square error (RMSE) of the current calculated for the sensors of each layer in each case is shown in Figure 8. It can be seen from the figure that the maximum RMSE of the current does not exceed 14 A, and the minimum RMSE is lower than 1 A. The RMSE of each phase current does not depend on the number of sensor layers, while the average RMSE of each layer of sensors gradually decreases. In Case 2 (as shown in Figure 8(b)), the current error calculated for the first layer of sensors is the largest, while the current error calculated

for the third layer of sensors is the smallest. Figure 9 shows the current values calculated for the first and third layer sensors in one cycle in Case 2, where the solid line represents the real current value of each phase line. It can be seen that although the RMSE of the current value calculated for the first layer sensor is relatively large, its calculation result still agrees well with the real current value. In Case 2, the maximum RMSE of each phase current value to the measurement current value range are 1.07, 1.14, and 1.19%, respectively, indicating that the algorithm proposed in this article is accurate.

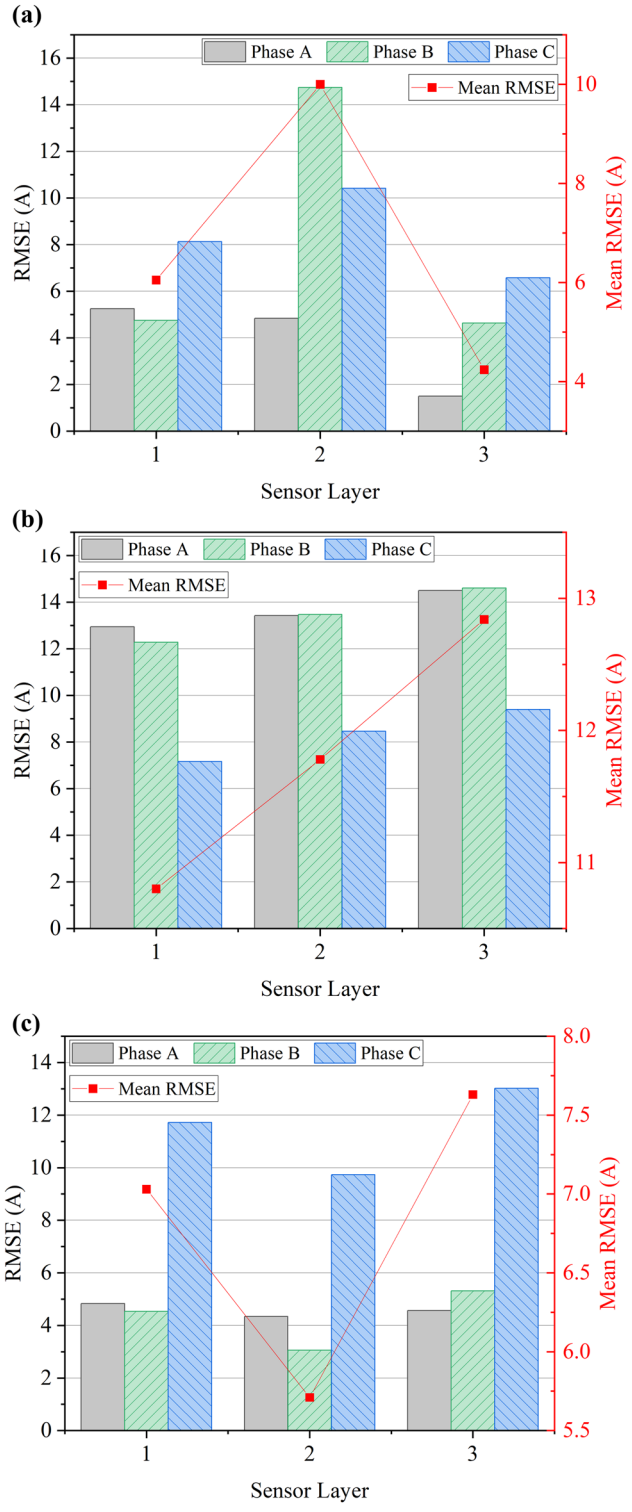

Figure 11: The RMSE and the mean RMSE calculated from each layer sensor in each case under unbalanced current: (a) Case 1, (b) Case 2, and (c) Case 3.

It is worth noting that the current numerical verification only samples 20 magnetic field values, which may affect the final calculation accuracy. Since increasing too many sampling points will increase the calculation time, in this article, 40 magnetic field values are sampled in one cycle with Δt = 0.5 ms, and the current-sag values of each phase line are calculated accordingly. Taking Case 2 as an example, the calculated sag of each phase line is shown in Table 4. It can be seen from the table that the relative error of the line sag does not improve significantly after increasing the sampling points. The RMSE of each layer of sensors is shown in Figure 10(a). It can be seen from the figure that the variation of the mean RMSE is different from Figure 8. The mean RMSE of the third layer sensor is the largest, which is 8.20 A, while the value of the first layer is 8.19 A. The current value calculated by the third layer sensors is shown in Figure 10(b). Compared with Figure 9(b), it can be seen that whether increasing the magnetic field sampling points or not, the calculated current value agrees well with the real value. According to the above analysis, it can be seen that the algorithm proposed in this article can reconstruct the balanced three-phase current and sag of the three-phase overhead line with fewer sampling points, and the calculation results are not sensitive to the sampling frequency.

In practical applications, most of the three-phase overhead lines have unbalanced currents, so it is necessary to carry out the verification and analysis of the unbalanced currents of the three-phase overhead lines. Three kinds of unbalanced currents are randomly selected for calculation. The sinusoidal current amplitudes and phases are shown in Table 5. The sags of each phase line are set to 7.4, 7.8, and 7.2 m, respectively. In one current cycle, 20 magnetic field values are sampled with Δt = 1 ms, and the sag of the line for the three cases is calculated based on these data points. The calculation results of the line sag for the unbalanced three-phase current are shown in Table 6. Compared with Case 2 of the balanced three-phase current (Table 3), it can be seen that the maximum relative error of the line sag calculated when the three-phase current is unbalanced has increased slightly, but the maximum relative error is less than 4%.

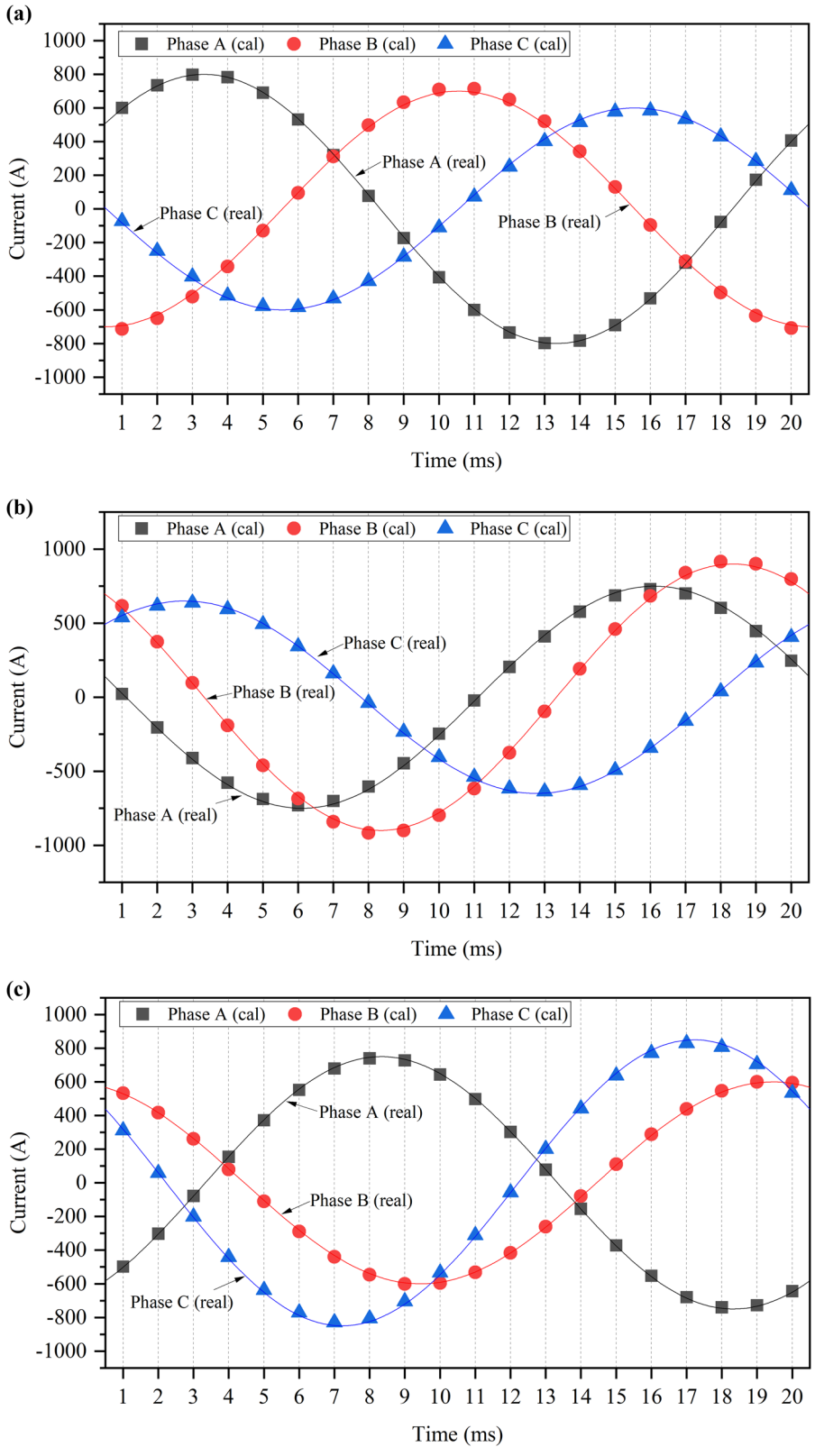

Figure 12: The calculated current of the sensor layer with maximum mean RMSE in each case under unbalanced current: (a) second layer in Case 1, (b) third layer in Case 2, and (c) third layer in Case 3.

Table 7: Error between the calculated amplitude of unbalanced current and real current

	Phase	Real value (A)	Calculated value (A)				Relative error (%)
			First layer	Second layer	Third layer	Mean	
Case 1	Phase A	800	792.7	801.4	802.0	798.7	−0.16
	Phase B	700	694.3	720.3	703.3	706.0	0.85
	Phase C	600	588.6	588.4	590.8	589.3	−1.79
Case 2	Phase A	750	731.9	731.3	729.8	731.0	−2.53
	Phase B	900	917.4	919.0	920.7	919.0	2.11
	Phase C	650	640.9	639.2	638.0	639.4	−1.64
Case 3	Phase A	750	743.2	743.9	743.5	743.5	−0.86
	Phase B	600	604.8	601.4	605.5	603.9	0.65
	Phase C	850	833.4	836.3	831.6	833.8	−1.91

Table 8: Error between the calculated initial phase of unbalanced current and real current

	Phase	Real value (°)	Calculated value (°)				Absolute error (°)
			First layer	Second layer	Third layer	Mean	
Case 1	Phase A	30	29.9	30.5	30.1	30.1	0.1
	Phase B	−100	−100.3	−100.4	−100.5	−100.4	0.4
	Phase C	−190	−189.9	−190.9	−190.1	−190.3	0.3
Case 2	Phase A	−200	−199.8	−199.8	−199.7	−199.8	0.2
	Phase B	120	120.1	120.0	120.0	120.0	0
	Phase C	40	39.6	39.5	39.5	39.5	0.5
Case 3	Phase A	−60	−60.0	−60.0	−60.0	−60.0	0
	Phase B	100	100.4	100.4	100.5	100.4	0.4
	Phase C	140	140.0	140.0	140.0	140.0	0

After calculating the sag, the DSM collects the sag values at each moment, and the CCM calculates the current values at each moment. Under the same sag of the line, the RMSE of the current of each layer sensor in the three cases is calculated, as shown in Figure 11. It can be seen from the figure that the RMSE of each phase current in each case does not depend on the number of sensor layers, and the variation of the maximum RMSE is random. The maximum RMSEs in each case are 14.74, 14.61, and 13.02 A, respectively. Compared with Case 2 of the balanced three-phase current condition, the error slightly increases when calculating the unbalanced three-phase current. In one cycle of current change, the current values of the sensor layer with the largest mean RMSE error in each case are calculated, and the calculation results are shown in Figure 12. It can be seen from the figure that the unbalanced current calculated by the algorithm proposed in this article still agrees well with the real current value and can reflect the waveform of the current change.

To make the current and phases obtained by the calculation more intuitive, the calculation results of the amplitude of the unbalanced three-phase currents are listed in Table 7, and the calculation results of the initial phases of the unbalanced three-phase currents are listed in Table 8. By comparing with the real values, it is found that the maximum relative error of the unbalanced current amplitude obtained by the calculation is 2.53%, and the maximum absolute error of the current initial phase is 0.5°. Therefore, the TMR sensor array and corresponding algorithm proposed in this article can accurately predict the sag and current of the three-phase overhead line.

5 Conclusions

This article studies the line current-sag state monitoring method by constructing the EMF theoretical model and simplified model of a 500 kV three-phase overhead line. The distribution of the magnetic field intensity under the three-phase overhead line, and the difference between the magnetic field obtained by the simplified model and the theoretical model were carefully analyzed. Then, the placement area of the TMR

sensor array below the line and the line current-sag were calculated and analyzed using the magnetic field simplified model. The main conclusions are as follows:

a) Under the three-phase overhead line with the same height of the suspension points of the same phase line, the distribution of the magnetic field intensity B is elliptical. The B_x value cannot be measured at $x = 0$ m; the B_y value cannot be measured at some positions in the region of $y \in (-5\text{ m}, 0\text{ m})$; in the line spacing range of $y \in (-13.2\text{ m}, 13.2\text{ m})$, the B_z value is not zero. In addition, on different height planes, the relative error between the magnetic field intensity value calculated by the simplified model and the theoretical model is small ($\delta < 0.75\%$) in the region of $x \in [-150\text{ m}, 150\text{ m}]$, but near the suspension point, the relative error is large ($\delta > 6\%$).
b) If the condition number is used as the evaluation criterion for the sensor placement area, when using a single-axis TMR magnetic sensor, the reasonable placement area of the y-axis sensor is $\{(x, y) \mid x \in (-200, 200), y \in (-5, 5)\}$, and the reasonable placement area of the z-axis sensor is $\{(x, y) \mid x \in (-200, 200), y \in (-10, 0) \cup (0, 10)\}$; when using a dual-axis TMR magnetic sensor, the reasonable layout area of the sensor is $y \in (-15\text{ m}, 15\text{ m})$.
c) If the sensor position sensitivity value is used as the evaluation criterion for the sensor placement area, the reasonable placement area of the y-axis sensor array is $\{(x, y) \mid x \in (-25, 25), y \in (0, 5)\}$, and the reasonable placement area of the z-axis sensor array is divided into two regions: $\{(x, y) \mid x \in (-125, 125), y \in (-13, -5) \cup y \in (3, 10)\}$. When using a dual-axis TMR magnetic sensor, the reasonable placement area of the sensor is $y \in (-10\text{ m}, 10\text{ m})$.
d) The relative error of sag calculated by the TMR sensor array and algorithm proposed in this article is less than 3% for the balanced current. The maximum RMSE of the current does not exceed 14 A, and the minimum RMSE is lower than 1 A under the balanced current; The relative error of sag calculated under the unbalanced current is less than 4%. The maximum RMSE of the current does not exceed 15 A. The relative error of the current amplitude is less than 3%, and the absolute error of the initial phase is less than 0.5°.

The results of this article are meaningful for the reasonable placement of magnetic field sensors under three-phase overhead lines and fast, accurate prediction of line current-sag.

Funding information: This work was supported by the S&T project of State Grid Corporation of China under grant number 52094021N00L.

Author contributions: All authors have accepted responsibility for the entire content of this manuscript and approved its submission.

Conflict of interest: The authors state no conflict of interest.

Data availability statement: The data that support the findings of this study are available from the corresponding author upon reasonable request.

References

[1] Douglass DA, Gentle J, Nguyen HM, Chisholm W, Xu C, Goodwin T, et al. A review of dynamic thermal line rating methods with forecasting. IEEE Trans Power Deliver. 2019;34(6):2100–9.
[2] Zainuddin NM, Abd Rahman MS, Ab Kadir MZA, Ali NHN, Ali Z, Osman M, et al. Review of thermal stress and condition monitoring technologies for overhead transmission lines: Issues and challenges. IEEE Access. 2020;8:120053–81.
[3] Chen YF, Ding XL. A survey of sag monitoring methods for power grid transmission lines. IET Gener Transm Dis. 2023;17(7):1419–41.
[4] Zuo J, Fan J, Ouyang Y, Liu H, Yang C, Hao CJ. Transmission line sag measurement and simulation research based on non-contact electric field sensing. Sensors. 2022;22(21):8379.
[5] Mukherjee M, Olsen RG, Li Z. Noncontact monitoring of overhead transmission lines using space potential phasor measurements. IEEE Trans Instrum Meas. 2020;69(10):7494–504.
[6] Ji YQ, Yuan JX. Overhead transmission lines sag and voltage monitoring method based on electrostatic inverse calculation. IEEE T Instrum Meas. 2022;71:1–12.
[7] Zhu K, Lee WK, Pong PWT. Non-contact capacitive-coupling-based and magnetic-field-sensing-assisted technique for monitoring voltage of overhead power transmission lines. IEEE Sens J. 2017;17(4):1069–83.
[8] Chen KL, Guo Y, Wang JC, Yang XG. Contactless islanding detection method using electric field sensors. IEEE Trans Instrum Meas. 2020;70:1–13.
[9] Xiao DP, He T, Zhao WH, Du XF, Xie YT. Improved three-dimension mathematical model for voltage inversion of ac overhead transmission lines. IEEE Access. 2019;7:166740–8.
[10] Vinh T, Jones TL, Shih CH. Magnetic fields near overhead distribution lines-measurements and estimating technique. IEEE Trans Power Deliver. 1991;6(2):912–21.
[11] Mamishev AV, Nevels RD, Russell BD. Effects of conductor sag on spatial distribution of power line magnetic field. IEEE Trans Power Deliver. 1996;11(3):1571–6.
[12] Filippopoulos G, Tsanakas D. Analytical calculation of the magnetic field produced by electric power lines. IEEE Trans Power Deliver. 2005;20(2):1474–82.
[13] McGuire T, Potter RL. Anisotropic magneto-resistance in ferromagnetic 3d alloys. IEEE Trans Magn. 1975;11(4):1018–38.
[14] Tian YF, Yan SS. Giant magnetoresistance: history, development and beyond. Sci China Ser G. 2013;56:2–14.
[15] Hewett T, Kusmartsev F. Extraordinary magneto-resistance: sensing the future. Open Phys. 2012;10(3):602–8.

[16] de Jong M. Recent progress in organic spintronics. Open Phys. 2016;14(1):337–53.
[17] Hirohata A, Takanashi K. Future perspectives for spintronic devices. J Phys D Appl Phys. 2014;47(19):193001.
[18] Yan SH, Zhou ZT, Yang YD, Leng QW, Zhao WS. Developments and applications of tunneling magneto-resistance sensors. Tsinghua Sci Technol. 2022;27(3):443–54.
[19] Khawaja AH, Huang Q, Li J, Zhang ZY. Estimation of current and sag in overhead power transmission lines with optimized magnetic field sensor array placement. IEEE Trans Magn. 2017;53(5):1–10.
[20] Khawaja AH, Huang Q. Estimating sag and wind-induced motion of overhead power lines with current and magnetic-flux density measurements. IEEE Trans Instrum Meas. 2017;66(5):897–909.
[21] Wu Y, Zhao G, Hu J, Ouyang Y, Wang SX, He JL, et al. Overhead transmission line parameter recon-struction for UAV inspection based on tunneling magnetoresistive sensors and inverse models. IEEE Trans Power Deliver. 2019;34(3):819–27.
[22] Xu Q, Liu XY, Zhu K, Pong PWT, Liu CH. Magnetic-field-sensing-based approach for current reconstruction, sag detection, and inclination detec-tion for overhead transmission system. IEEE Trans Magn. 2019;55(7):1–7.
[23] Chen KL. Intelligent contactless current measurement for overhead transmission lines. IEEE Trans Smart Grid. 2022;13(4):3028–37.
[24] Xiang Y, Chen K, Hong Z, Jiang Z. Contactless HVDC current measurement method using TMR-based sensors. Electr Power Autom Equip. 2020;40(4):185–90.
[25] Mujezinović A, Dautbašić N, Dedović MM. More accurate 2D algorithm for magnetic field calculation under overhead transmission lines. In: Avdakovic S, Mujcic A, Mujezinovic A, Uzunovic T, Volic I, editors. Advanced Technologies, Systems, and Applications IV-Proceedings of the International Symposium on Innovative and Interdisciplinary Applications of Advanced Technologies, Sarajevo, Bosnia-Herzegovina, 20–23 June 2019. Springer; 2020. p. 345–54.
[26] Riba Ruiz JR, Garcia Espinosa A. Magnetic field generated by sagging conductors of overhead power lines. Comput Appl Eng Educ. 2011;19(4):787–94.
[27] Budnik K, Machczyński W. Contribution to studies on calculation of the magnetic field under power lines. Eur Trans Electr Power. 2006;16(4):345–64.
[28] Khawaja AH, Huang Q, Khan ZH. Monitoring of overhead transmission lines: A review from the perspective of contactless technologies. Sens Imaging. 2017;18(1):1–18.